



A laboratory study of channel sidewall expansion in upland concentrated flows

Chao Qin^{a,b,c}, Fenli Zheng^{a,d,*}, Robert R. Wells^c, Ximeng Xu^{a,b}, Bin Wang^e, Keyuan Zhong^a

^a Institute of Soil and Water Conservation, State Key Laboratory of Soil Erosion and Dryland Farming on the Loess Plateau, Northwest A & F University, Yangling 712100, Shaanxi, PR China

^b National Center for Computational Hydroscience and Engineering, University of Mississippi, Oxford 38655, MS, USA

^c USDA-ARS National Sedimentation Laboratory, Oxford 38655, MS, USA

^d Institute of Soil and Water Conservation, CAS & MWR, Yangling 712100, Shaanxi, PR China

^e School of Soil and Water Conservation, Beijing Forestry University, Beijing 100083, PR China

ARTICLE INFO

Keywords:

Gully erosion
Photogrammetry
Basal scour
Tension crack
Non-erodible layer

ABSTRACT

Gully erosion contributes large amounts of sediment within watersheds around the world. Gully widening constitutes about 80% of total soil loss, especially in the presence of a plow pan which manifests a less or non-erodible soil layer. Current knowledge on sidewall toe scour (scour arcs) and tension crack processes in gully widening is limited. Thus, simulated channel sidewall expansion tests, where the channel bed was fixed to represent a non-erodible layer, were designed to investigate how inflow rate, slope gradient and initial channel width affect channel widening processes. Soil boxes (2.0 m-long, 0.3 m-wide and 0.5 m-deep) with two slope gradients (15° and 20°), four inflow rates (1.0, 2.0, 3.0 and 4.0 L min⁻¹) and two initial channel widths (4 and 8 cm) were subjected to clear-water overland flow. Photogrammetry was used to detect tension crack and width variations of channels. The results show that sediment delivery and channel width increase with the increase of inflow rate, bed slope and the decrease of initial channel width. Exponential equations were used to predict the channel width time series. Time lag occurred between sediment peak and soil block failure. Toe scour, crack development, sidewall failure and block detachment and transport, in sequence, were the four main processes of channel widening. Basal scour arc length, tension crack length and width decreased with initial channel width and increased with time, flow discharge and bed slope. Basal scour arcs were divided into three patterns according to different shapes in comparison to the failure arcs. Sediment delivery equations based on the disaggregation of concentrated flow entrainment and mass failure were also fitted. This study provides new insight on improving gully erosion measurements and prediction technology.

1. Introduction

Gully erosion, where runoff water accumulates and removes soils from the gully area, is one of the main soil erosion types and a major source of sediment to river systems (FAO, 1965). Depending on morphological characteristics and erosion patterns, gullies can be divided into two types: ephemeral gully and classical gully (Foster, 1986; Castillo and Gómez, 2016). Soil loss by gully erosion represents from 10% to 94% of total water erosion worldwide and it occupies around 60% of the sediment yield in the hilly gully region and more than 80% in the gully region on the Loess Plateau of China (Poesen et al., 2003). Concentrated flow in gully channels erodes fertile soil and fragments croplands, and as a result, gullies become pathways for transporting other pollutants within watershed systems (Castillo and Gómez, 2016).

Physical gully evolution processes include headcut migration, bed incision and sidewall expansion (widening), and each process dominates at different phases of gully development (Bingner et al., 2016). These three processes occur consecutively and interact with each other through feedbacks. Initial gully width is determined by the gully head retreat process. When a non- or less-erodible layer is present in the subsurface in a constant bed slope gully, the concentrated flow begins to erode the base of sidewalls and, consequently, increased gully widening follows (Di Stefano and Ferro, 2011; Wells et al., 2013). Chaplot et al. (2011) reported that sidewall retreat was confirmed to be a main process after headward migration in overall gully evolution and overall erosion in landscapes. Sidewall failure, which provides the main sediment source during the final stage of gully development, contributes as much as 80% of the total eroded sediment from incised

* Corresponding author at: No. 26, Xi'nong Road, Institute of Soil and Water Conservation, Yangling 712100, Shaanxi, PR China.

E-mail addresses: flzh@ms.iswc.ac.cn (F. Zheng), Robert.Wells@ars.usda.gov (R.R. Wells), xuxm@nwsuaf.edu.cn (X. Xu), wangbin1836@bjfu.edu.cn (B. Wang), zkygeo@163.com (K. Zhong).

<https://doi.org/10.1016/j.still.2017.12.008>

Received 7 April 2017; Received in revised form 10 November 2017; Accepted 7 December 2017

0167-1987/ © 2017 Elsevier B.V. All rights reserved.

channels in the loess area of the Midwest United States (Simon et al., 1996) and more than half of the gully volume in New South Wales, Australia (Blong et al., 1982). Various factors such as discharge, slope, soil properties and management conditions significantly influence gully width evolution processes (Bingner et al., 2016). Wells et al. (2013) pointed out that gully width and its widening rate increased as bed slope and discharge increased and corresponding predictive empirical equations of gully widening were formulated.

The processes and mechanisms of gully sidewall collapse are complex and attract much attention (Martinez-Casasnovas et al., 2004; Chaplot et al., 2011; Chen et al., 2013; Wells et al., 2013; Momm et al., 2015; Bingner et al., 2016). However, the failure of gully sidewalls is hard to be fully evaluated because it is influenced by many factors (Bradford and Pies, 1977). Istanbuluoglu et al. (2005) pointed out that gully erosion is most commonly triggered by fluvial erosion, more specifically, the bank failure is attributed to a combination of water erosion (fluvial shearing process) and gravity erosion effects (gravitational mass failure process). Chaplot et al. (2011) indicated that the triggering of gully sidewall failure processes could be attributed to three sub-processes which contribute to total gully sidewall erosion in descending order: by water running along gully sidewalls, transport of soil material by splash and the falling of entire soil blocks. Gravitational mass failure, which is difficult to predict due to its sudden occurrence, begins with sidewall toe scour, ultimately leading to high and unstable sidewalls (Chen et al., 2013). After scouring the gully toe, a tension crack frequently forms on the surface behind the sidewall top lip. These cracks occur when the driving forces, e.g., gravitational force, become larger than the resisting forces, i.e., soil cohesion and friction (Istanbuluoglu et al., 2005; Thomas et al., 2009). The overhanging layers then continue being undermined by fast concentrated flows, and as a result, collapse and gully widening accelerate (Billi and Dramis, 2003; Martinez-Casasnovas et al., 2004; Chen et al., 2013).

Non-erodible layers, which have a resistance to erosion greater than that of the overlying soil, often develop due to conventional tillage operations (Wells et al., 2013). The plow depth is often correlated with depth to the non-erodible layer, as the lower edge of the plow or disc tends to compact and smear the soil at that depth. As soil erodes and concentrated flow occurs, incision through the freshly ploughed soil is delayed or halted at the intersection of the plow pan and the above erodible layer (Bingner et al., 2016). Gully widening occurs as a consequence of this intersection and shows an increase in widening rate, as the energy of the flowing water shifts from a vertical force to a horizontal force. Researches on rill and gully erosion, have focused on the sidewall widening processes and mechanisms when plow pans were encountered, and indicated that a platy-structured compact bed which is a less- or non-erodible layer was often formed at the plough depth (Fullen, 1985; Shen et al., 2015). Laboratory studies were designed to investigate the impact of non-erodible layer on gully evolution, especially gully widening (Gordon et al., 2007; Wells et al., 2013).

Research findings on river bank toe-erosion process and its affecting factors (Wang et al., 2016), tension crack formation and development (Hossain et al., 2011), mass failure mechanisms (Darby et al., 2002; El Kadi Abderrezzak et al., 2014) and bank stability simulation (Darby et al., 2002) have laid a foundation for gully sidewall collapse research. However, some of the algorithms that have been developed to determine river/gully width have not taken depth limitation into account so that it may significantly impact the widening prediction where a less erodible layer encountered (Gordon et al., 2007; Wells et al., 2013; El Kadi Abderrezzak et al., 2014; Bingner et al., 2016). The processes that control gully widening such as sidewall toe scour and changes of tension crack with time is still very weak and need to be intensified (Bingner et al., 2016). Understanding of gully bank retreat should be considered by further in-situ and modeling studies (Chaplot, 2013). Improved understanding of gully widening processes is critical to the development of some modules of water erosion prediction models such as CREAMS, EphGEE and AnnAGNPS (Wells et al., 2013; Dabney et al.,

2014; Bingner et al., 2016) and is essential in the assessment of conservation practices on controlling gully erosion in agricultural fields.

In this study, channels are formed above a non-erodible layer to investigate channel widening processes with certain inflow volume and varied durations after channel headcut migrating upstream and channel bed finishing undercutting. Scouring tests were implemented to study the effect of slope gradient, inflow rate and initial width on channel widening in the presence of a non-erodible channel bed. The specific objectives of this study were: 1) to determine channel sidewall expansion processes and morphodynamic changes under different experimental designs, 2) to discuss how channel toe scour and tension crack development affect the channel widening process, and 3) to establish a predictive equation for channel width time series.

2. Materials and methods

2.1. Experimental design, materials and setup

This study consisted of 12 experimental runs (non-completely orthogonal experimental design), three factors were considered: four inflow rates (1.0, 2.0, 3.0, 4.0 L min⁻¹), two slope gradients (15° and 20°) and two initial channel widths (4 and 8 cm width with 4 cm depth). The lengths of different experimental runs were in accordance with inflow rates to keep the total inflow volume constant (60 L). For 1.0, 2.0, 3.0 and 4.0 L min⁻¹ inflow rate, the lengths of experiments were 60, 30, 20 and 15 min, respectively. Each experimental run included two replicates and the experiments reported here are average values of these two replicates; however, the 8-cm initial channel width was tested with the 20° slope only. The detailed comparisons between experimental design and natural conditions is shown in Table 1 (Zhang, 1983; Zhou and Wang, 1987; Wu and Cheng, 2005; Wang et al., 2014). Four soil boxes measuring 2.0 m-long, 0.3 m-wide and 0.5 m-deep (Fig. 1), containing drain holes with 2 mm diameter (1 cm grid spacing) at the soil box bottom, were used in this study. For each experimental run, soil boxes were selected randomly to prevent the occurrence of systematic error. A runoff outlet at the downstream end of the soil box was used to collect runoff samples throughout the experiment (Fig. 1). A down sprinkler rainfall simulation system (He et al., 2014), consisted of three nozzles, can be set to a range of 30–350 mm h⁻¹ rainfall intensity. Flow discharge was controlled by a constant-head water tank fixed 2.5 m above the soil box. To ensure that the regime of concentrated flow entering the initial channel was laminar, energy dissipation practices were applied at the transition section. It was a simulation of the changing process of turbulent flow with high flow velocity of channel headcut to laminar flow with low flow velocity of channel body. Pebbles of different sizes were pasted at the water tank outlet and linen cloth was laid at the junction between water tank and soil box (Fig. 1). Flow energy was dissipated and flow velocity was controlled at the transition section. The adjustable range of inflow rate was

Table 1
Comparisons of gully channels on the Loess Plateau and simulated channels, characteristics of rainfall and topography between natural conditions and experimental design.

Factors	Natural condition	Experimental design
Erosive rainfall intensity (equivalent inflow rate)/mm h ⁻¹	10.5–234.8	10, 20, 30, 40
Erosive rainfall duration (experiment length)/min	5–600	15, 20, 30, 60
Slope gradient/°	15–39	15, 20
Width depth ratio	0.24–1.47	1, 2
Less- or non-erodible layer	Plow pan	Non-erodible layer
Depth of non-erodible layer/cm	20–40	4
Soil bulk density/g cm ⁻³	0.93–1.85	1.1 for plow layer, 1.3 below plow layer

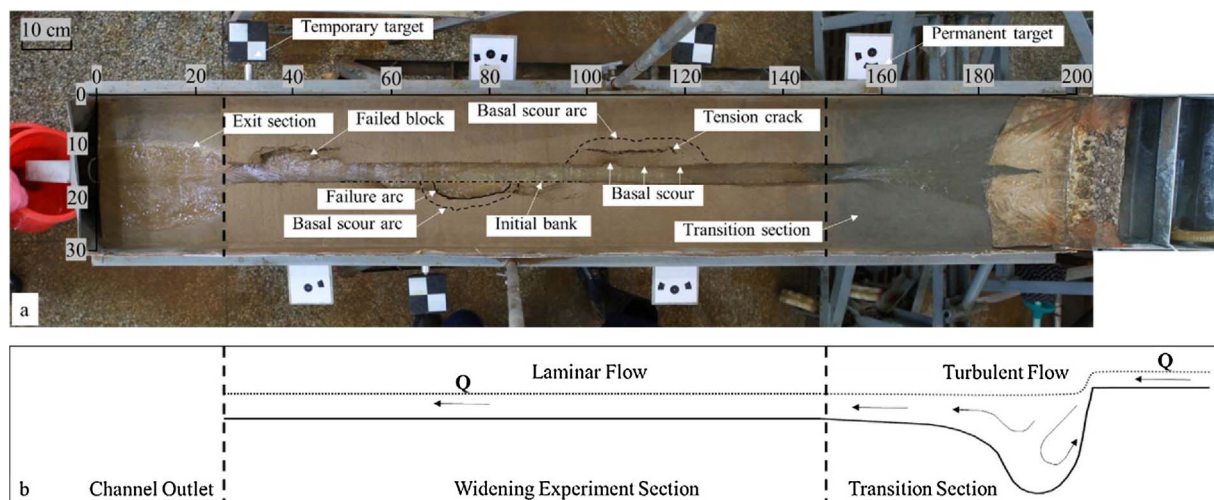


Fig. 1. a) Photo of the experimental facility and describing indicators for channel widening processes, and b) Sketches of the simulated transition section, widening experiment section and channel outlet.

Table 2
Summary of experimental parameters and basic information.

Run	Bed slope (°)	Inflow rate (L min ⁻¹)	Inflow duration (min)	Initial channel length (cm)	Initial channel width (cm)	Channel widening rate (cm min ⁻¹)	Flow velocity (cm s ⁻¹)	Runoff rate (L min ⁻¹)		Sediment delivery (kg)		Unit channel width sediment delivery (kg m ⁻¹)	
								Avg	SD	Avg	SD	Avg	SD
1	15	1	60	143.4	4.1	1.6×10^{-2}	51.6	0.96	0.04	0.74	0.10	16.15	2.19
2	15	2	30	144.1	4.0	6.6×10^{-2}	72.7	1.92	0.04	1.04	0.02	20.87	0.36
3	15	3	20	141.6	4.1	1.5×10^{-1}	76.7	2.94	0.02	1.52	0.20	27.22	3.59
4	15	4	15	138.1	4.0	2.8×10^{-1}	79.6	3.81	0.06	2.10	0.30	34.92	4.93
5	20	1	60	151.6	4.0	2.3×10^{-2}	59.6	0.96	0.02	0.98	0.03	20.95	0.57
6	20	2	30	145.5	4.1	6.9×10^{-2}	74.8	1.97	0.03	1.21	0.13	23.73	2.62
7	20	3	20	147.4	3.9	1.8×10^{-1}	79.2	2.88	0.07	1.76	0.21	30.95	3.67
8	20	4	15	145.3	4.1	3.1×10^{-1}	82.7	3.85	0.08	2.25	0.25	35.19	3.91
9	20	1	60	150.8	8.0	1.6×10^{-2}	52.1	0.96	0.03	0.73	0.20	8.58	2.39
10	20	2	30	148.9	8.1	5.6×10^{-2}	67.4	1.98	0.03	0.99	0.18	11.12	1.99
11	20	3	20	148.7	8.0	1.4×10^{-1}	75.8	2.92	0.00	1.46	0.12	15.40	1.27
12	20	4	15	145.1	8.0	2.6×10^{-1}	77.6	3.92	0.02	1.90	0.29	18.95	2.93

0–10 L min⁻¹. A summary of experimental parameters is given in Table 2.

The soil used in this study was loess (fine-silty and mixed), which can be classified as a *Calcic Cambisol* (USDA NRCS, 1999). The top 20 cm of the Ap horizon was collected at a well-drained site in Ansai County (36°45'N, 109°11'E), which is located in the hilly gully region of the Loess Plateau in Shaanxi Province, Northwest China. The soil texture was 28.3% sand (> 50 μm), 58.1% silt (50–2 μm), 13.6% clay (< 2 μm), and contained 5.9 g kg⁻¹ soil organic matter. The methods used to analyze soil texture and soil organic matter were the pipette method (Hunt and Woolf, 1969) and the potassium dichromate oxidation-external heating method (Liu, 1996), respectively. The soil was sieved through a 0.25-mm sieve but not oxidized prior to soil texture analysis. The soil pH in water (1:2.5 solid-to-water ratio, weight basis) was 7.95. Impurities, such as large organic matter and gravel, were removed from the soil, and the soil was passed through a 5-mm sieve prior to packing the boxes.

2.2. Experimental procedures

2.2.1. Preparation of soil box

Before packing the soil box, the soil water content was determined and used to calculate how much soil was needed for packing. The soil box was filled from the bottom to the top with sand and soil material. The detailed steps of preparing the soil box and design basis are: 1) The

lower 10 cm of the soil box was filled with sand to allow free drainage of excess water (Shen et al., 2015). 2) A highly permeable cloth was used to separate the sand and soil layers (Shen et al., 2015; Wells et al., 2013). 3) Soil (11–13 g 100 g⁻¹ soil water content) was packed above the permeable cloth in 0.05 m increments with a 1.30 g cm⁻³ soil bulk density (BD) and a total depth of 25 cm (Shen et al., 2015; Wells et al., 2013). The soil depth and BD of this layer can be flexible due to the erosion process only occurring above the non-erodible layer. Each packed soil layer was lightly raked for homogeneity before placing the next layer. The amount of soil in each layer was kept as constant as possible to maintain a similar soil bulk density and a uniform spatial distribution. 4) A 0.01 m non-erodible layer with a 1.30 g cm⁻³ soil bulk density, whose strength was large enough to resist the concentrated flow, was placed above the 25-cm soil layer. This layer consisted of a 5 to 3 mixture of soil and cement (Wells et al., 2013). Field measurements of BD on the sloping croplands in Ansai County showed that BD of plow pan varies between 1.28 and 1.39 g cm⁻³. The designed BDs also corresponded with those of Wang et al. (2014) obtained from field measurement (0.93–1.85 g cm⁻³) on the Loess Plateau and Shen et al. (2015) in laboratory studies (1.35 g cm⁻³ for plow pan) of the Loess soil. 5) The non-erodible layer was then sprayed with water until surface ponding occurred (Gordon et al., 2007). To cure the non-erodible layer, a fan forced air over the surface for 24 h 6) A 4-cm top erodible layer with a 1.10 g cm⁻³ soil bulk density was packed above the non-erodible layer. The depth of the top erodible layer was designed

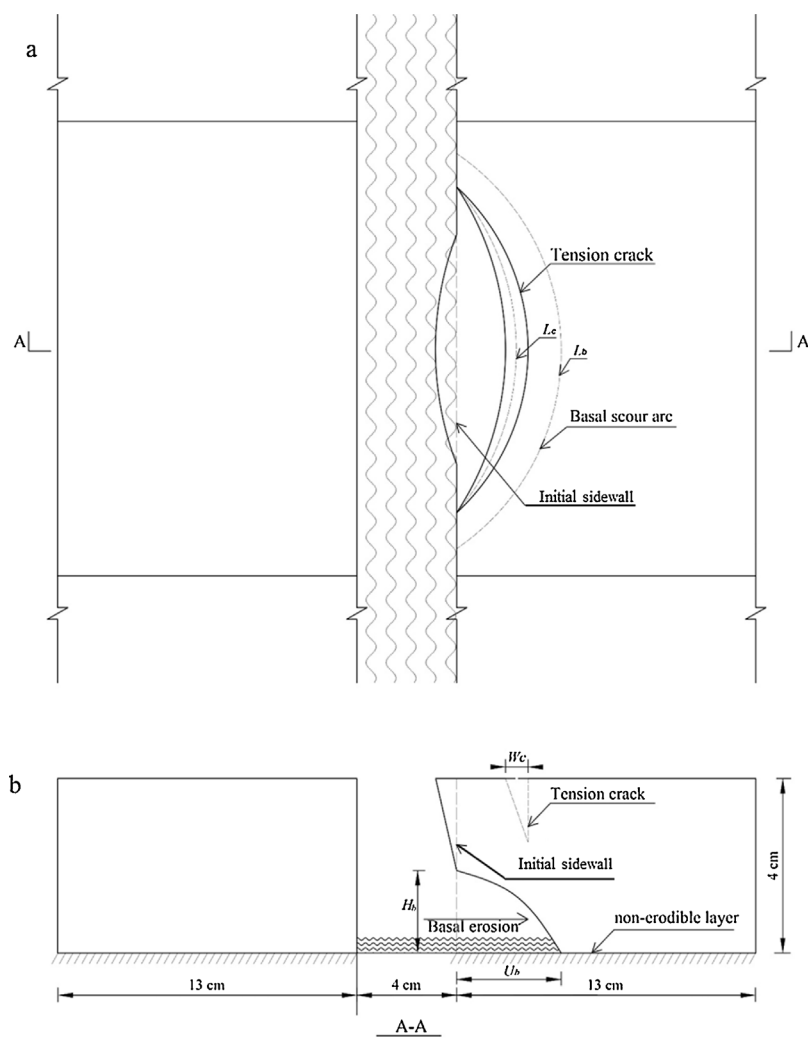


Fig. 2. Sketches of: a) top view of channel sidewall (show tension crack, basal scour arc length (L_b) and crack length (L_c)), and b) profile of channel sidewall (show tension crack, basal undercutting (U_b), basal scour height (H_b) and maximum crack width (W_c)).

according to Wells et al. (2013). The BD of this layer was designed according to the field measurement ($1.01\text{--}1.15\text{ g cm}^{-3}$) and former studies of Shen et al. (2015) and Wang et al. (2016). 7) Then, a 4 or 8 cm width initial channel was excavated down to the non-erodible layer. Two string lines were clipped at the boundary of the soil box as a baseline for excavating. Rectangular-shape metal channel models, measuring 140 cm length, 4 or 8 cm width and 4 cm height, with sharp edges were inserted into the plow layer. Then the redundant soil was carefully removed from the channel. 8) The transition section between the inlet tank and the soil cavity was formed and stabilized with cement (Fig. 1).

Then, a 30-mm h^{-1} pre-rain was applied for 30 min to the soil bed set at 3° slope gradient. The total rainfall amount was 15 mm. This ensured that no water ponded on the soil surface. The purpose of the pre-rain was to develop consistent soil moisture, consolidate loose soil particles by raindrop impact, and reduce the spatial variability of underlying soil conditions. After a 12 h period to allow soil water redistribution, the bed slope was adjusted to the designed experimental slope gradient (15° or 20°).

2.2.2. Experimental procedures

Before the experiment, the inflow rate was calibrated to the target flow rate. After feeding the concentrated inflow, the runoff and sediment from the test sample were captured in 5 L plastic buckets at 30 s intervals. Sediment samples were weighed, settled (24 h storage), transferred into 0.5 L aluminum boxes and dried in an oven at 105°C

for 24-h, then reweighed. Characteristics of concentrated flow and channel toe scour were measured in 2-min intervals during the experiment. Specifically, flow velocity was measured by KMnO_4 dye tracing method at slope lengths of 40 to 90 and 110 to 160 cm, flow depth was measured by electronic gauge pin at the center bottom of channel (TD-SX40-1, 0.1 mm measuring resolution, 0.3 mm maximum error when measuring depth is < 200 mm), and flow width was measured with a steel ruler. Channel toe scour characteristics (basal undercutting, arc length and height) were measured with a soft ruler.

Photogrammetry was used to capture the characteristics of channel widening and micro-distortion of the soil surface. At slope lengths of 70 and 120 cm, two cameras (Canon EOS 5D Mark II) were mounted 1.5 m above the soil bed. Similar to the method developed by Wells et al. (2013) and Momm et al. (2015), four permanent and three temporary targets (used for a complementary of the targets' reflection and shelter) parallel to soil surface were setup at the boundary of the soil box (Fig. 1). The total station was used to measure the exact coordinates of each target. Cameras were set to the appropriate position which could ensure that photos were parallel to the soil surface and overlapped each other. Cameras were fixed on a stable steel shelf and no tilt shift was applied during the experiment. Then, adjustments were made to both cameras: 1) set shooting type as RAW with the highest camera resolution (2720×4080); 2) selected manual scene mode, set appropriate aperture ($f/2.8$), ISO (250) and shutter speed ($1/20$ s) and kept them constant during each run; 3) focused automatically until clear photos obtained, then set focus mode as manual focus (MF), focal length

(24 mm) was kept constant during each run.

During the experiment, the cameras were controlled by an infrared remote control and photos were taken simultaneously at 30 to 60 s intervals. The interval was reduced to 10 s during the primary erosion period. Photos were imported into Agisoft Photoscan Professional 1.2.4 (Agisoft LLC, St. Petersburg, Russia) after each run. Dense point cloud data were exported with .txt format after a series of preprocessing operations (including target detection, photo alignment, coordinate transformation and matching). The exported point clouds data were then imported into ArcGIS 10.4 (ESRI Inc., Redlands, CA, USA) to construct digital elevation models (DEMs) (Momm et al., 2015). The processes of constructing DEMs included making an x, y event layer; creating a triangulated irregular network (Tin) and a fishnet of rectangular cells; performing spatial adjustment; recreating Tin; and Tin to raster. The interpolation used was natural neighbors. The resolution of DEM was averaged to a 5 mm × 5 mm raster grid. Channel width at each time phase was calculated based upon the average channel widths of parallel and equally spaced cross-section lines at 0.02 m. The calculation process is similar to that used by Momm et al. (2015). A total of 48 to 54 channel widths were measured and averaged for a final channel width. Length and width of each crack were measured separately throughout the flume using DEMs produced from the photogrammetry.

2.3. Indicators for describing channel widening processes and mechanisms

Eight indicators were chosen to describe channel widening processes (Figs. 1 and 2):

- 1) Basal undercutting (cm, U_b): measured with a soft steel ruler, average undercut distance of 3 to 6 measurements parallel to the channel bed of one scour arc;
- 2) Basal scour arc length (cm, L_b): simulated by a fitted polynomial, the length of multiple basal undercutting measurements at different positions along the toe;
- 3) Basal scour height (cm, H_b): measured with a soft steel ruler, average height of 3 to 6 measurements of one scour arc;
- 4) Crack length (cm, L_c): measured by photogrammetry;
- 5) Crack lengthening rate (cm min^{-1} , V_{cl}): measured by photogrammetry, crack length by time from crack formation to failure;
- 6) Crack width (cm, W_c): measured by photogrammetry, average crack width of 3 to 6 measurements of one crack;
- 7) Crack widening rate (cm min^{-1} , V_{cw}): measured by photogrammetry, crack width by time from crack formation to failure;
- 8) Failed block surface area (cm^2 , A_s): measured by photogrammetry at the moment of failure;
- 9) Channel widening rate (cm min^{-1} , V_{ch}): measured by photogrammetry, channel width changes in time.

2.4. Data analysis

Sampling errors occur due to the fact that the sample does not include all members of the population while the statistical characteristics of a population need to be estimated from a sample (Särndal et al., 1992). In order to minimize sampling error caused by different numbers of failure and scour arcs, eight selected basal scour examples and cracks were selected from left and right sidewalls, respectively for each experimental treatment (including two replicate runs). The description and analysis of all basal scours, tension cracks and failed blocks were the average values of these eight selected examples.

The determination coefficient (R^2) and the Nash-Sutcliffe simulation efficiency (E_{NS}) (Nash and Sutcliffe, 1970) were used to evaluate the prediction accuracy of the equations. If the values of R^2 and E_{NS} are close to 1, the model prediction is considered 'perfect'. Typically, when $R^2 > 0.6$ and $E_{NS} > 0.5$, the equation prediction is acceptable or satisfactory (Santhi et al., 2001).

3. Results and discussion

3.1. Runoff and soil loss

Concentrated flow depths were in the order of 0.05 to 0.18 cm, flow velocities varied from 51.6 to 82.7 cm s^{-1} and flow widths varied based on basal scouring and channel widening (Table 2). Runoff rates were 2.4% to 5.7% lower than those of calibrated inflow rates, which can be attributed to infiltration through the non-erodible layer and water absorption into the channel sidewalls. Sediment delivery increased by 22.9% to 40.5% when inflow rate increased from 1 to 2 L min^{-1} , while it increased by 86.1% to 100.8% when inflow rates increased from 2 to 4 L min^{-1} . Sediment delivery increased by 7.5% to 32.6% when slope gradient increased from 15° to 20°. But sediment delivery decreased by 15.8% to 25.9% when channel width increased from 4 to 8 cm. Table 2 shows that unit sediment delivery with 8 cm initial channel width was 46.1% to 59.0% lower than that with 4 cm initial channel width. The reason is that flow in narrower channels was more concentrated with higher flow depth, velocity, shear stress and, eventually, resulted in lower sediment delivery with 8 cm initial width.

3.2. Response of sediment processes to channel widening processes

3.2.1. Sediment processes

The sediment delivery time series are shown in Fig. 3. The panels are organized by initial channel width and slope gradient, with the data for each of the four flow rates shown in each panel. The results show that flow rate, slope and channel width all played major roles in sediment delivery. In general, sediment delivery was characterized by an initial low transport period, in which sediment delivery was relatively low, followed by a high transport period (dashed lines in Fig. 3). As

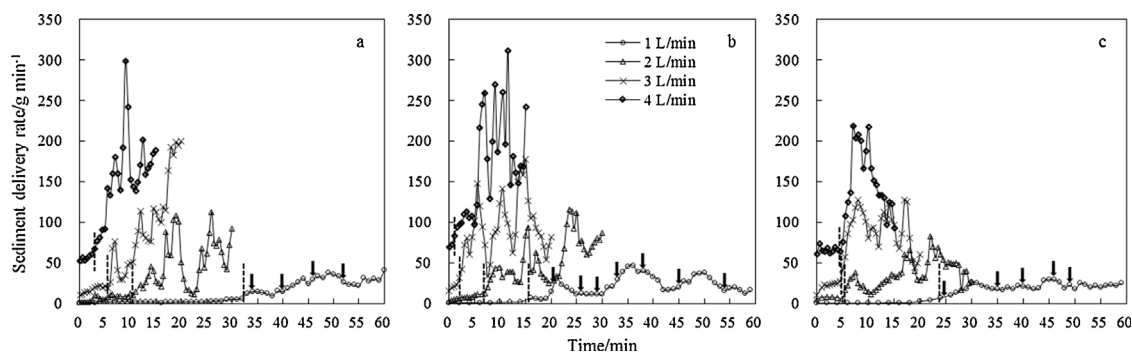


Fig. 3. Time series of sediment delivery for (a) 4 cm initial channel width at 15° slope gradient, (b) 4 cm initial channel width at 20° slope gradient and (c) 8 cm initial channel width at 20° slope gradient (dashed lines represent the turning points between initial low transport periods and high transport periods in all treatments; closed arrows represent the timing of initial sidewall failure of 1 L min^{-1} treatment series).

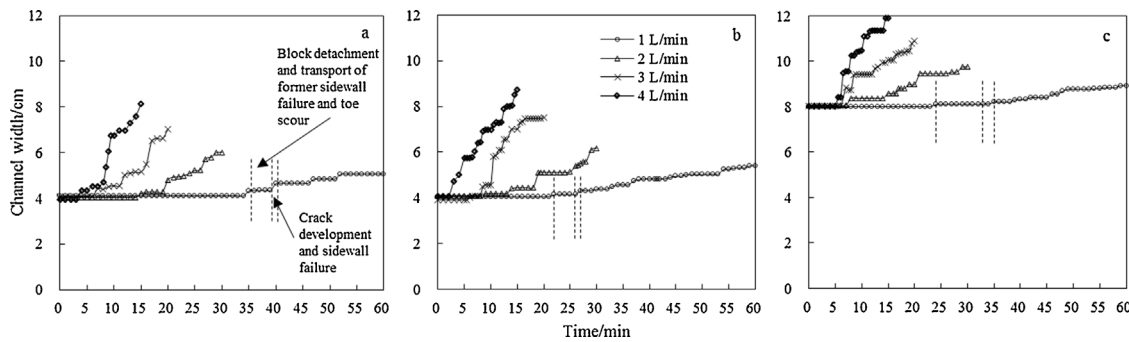


Fig. 4. Time series of channel width for (a) 4 cm initial channel width at 15° slope gradient, (b) 4 cm initial channel width at 20° slope gradient and (c) 8 cm initial channel width at 20° slope gradient (dashed lines are boundaries between block transport and toe scour, and crack development and sidewall failure of 1 L min⁻¹ treatment series).

flow rate and slope increased, the timing of the high transport period became earlier in the experiment (Fig. 3a, b). And, as the initial channel width increased, the duration of the low transport period prolonged (Fig. 3b, c). For example, the timing of the low transport period shortened from 32.5 to 4.5 min (4 cm initial channel width under 15° slope; Fig. 3a) as the flow discharge increased from 1 to 4 L min⁻¹, respectively, and decreased from 32.5 to 16 min with an increase in slope (15° to 20° under 1 L min⁻¹; Fig. 3a, b). During the high transport period, plateaus in sediment concentration occurred during the intervals between sidewall failures. The sediment delivery fluctuated more for the larger slope with higher flow rates and smaller initial channel width (Fig. 3a–c).

3.2.2. Channel widening processes

The average channel width time series is shown in Fig. 4. At a given slope and initial channel width, flow rates influenced channel widening. As initial channel width decreased, flow rate and slope increased, the channel widened faster (Table 2). Channel widening rate increased by 0.9 to 3.1 times when inflow rate increased 1 L min⁻¹ while it increased by 4.5% to 43.8% and 16.1% to 30.4% when bed slope increased from 20° to 25° and initial channel width decreased from 8 to 4 cm, respectively. The results indicated that the increase of inflow rate has the most important effect on the channel widening process. At the lowest inflow rate, steeper slope, and narrower initial channel width, the timing of channel expansion began earlier (from 35 to 22 min under 1 L min⁻¹; Fig. 4a, b); although similar channel expansion initiation points were observed for 4 cm initial channel width under 15° slope and 8 cm initial channel width under 20° slope at the lowest flow rate (Fig. 4a, c). Channel expansion started earlier as the flow rate and slope increased. The timing of channel expansion was similar for the 8-cm initial channel width and flow rates above 1 L min⁻¹ (Fig. 4c). The trend of channel width fluctuated and frequently plateaued during the high transport period. The ultimate channel width increased from 5.1 to 8.1, 5.4 to 8.8 cm for 4 cm initial channel width at 15° and 20° slope, and 8.9 to 11.9 cm for 8 cm initial channel width under 20° slope (Fig. 4).

Exponential equations were chosen to describe the channel width time series. The coefficients of determination (R^2) increase with the increase of inflow rate and initial channel width and, they are greater than 0.65 for all runs. The high coefficients of determination suggested that an exponential function may be used to simulate the channel widening processes on steep Loess hillslopes. Therefore, the channel width may be described by

$$W = Ae^{BT} \quad (1)$$

where W (cm) is channel width, A and B are parameters related to initial channel width (W_i), upslope inflow rate (Q) and slope gradient (S). The coefficient A may be represented by the initial channel width, W_i , while the exponent B may be modeled using Q and S . The exponent B

was fitted as a power function depending upon Q and S . Three quarters of the data (Run 1, 3, 4, 5, 6, 8, 9, 11 and 12) were used to fit the equations while another one quarter (Run 2, 7 and 10) was used for equation verification. The parameter B is given by

$$B = 0.0617(QS)^{1.859} \quad (R^2 = 0.846, P < 0.005, n = 9) \quad (2)$$

Substituting Eq. (2) into Eq. (1), yields:

$$W = W_i e^{0.0617(QS)^{1.859}T} \quad (3)$$

The verification of Eq. (3) indicated that the determination coefficient (R^2) and the Nash-Sutcliffe simulation efficiency (E_{NS}) were 0.882 and 0.874, respectively. This validation result shows that the equation fitted in this study attains a satisfactory level of accuracy and its prediction results are acceptable (Santhi et al., 2001).

The exponential relationship between time series and channel width and, the occurrence of plateau-surge pattern verified the results given by Foster et al. (1980) and Wells et al. (2013), who indicated that channel width can be predicted using exponential equations of initial channel width and time. Dispersion of soil particles by concentrated flow dominated the low transport period. Surge period, which was equal to less than one-fifth duration of the low transport period, contributed large amounts of the sediment delivery to total soil loss. Fluvial erosion has been proven to form a linear erosion (Chaplot et al., 2011), while the combination of fluvial erosion and fall down of aggregates make the channel widening process complex and tend to behave in the form of an exponential relationship.

3.2.3. Response of sediment delivery to channel widening processes

Sediment delivery reflected the channel widening process. The duration of the low and high transport periods of sediment delivery also corresponded to channel widening processes. The results show that when channel width was constant from 2 to 35 min of different runs, which occurred at 4 L min⁻¹ under 20° slope and 1 L min⁻¹ under 15° slope, respectively, in Fig. 4a and b, sediment delivery rate varied at a low level from 1.5 to 32 min, which occurred at 4 L min⁻¹ under 20° slope and 1 L min⁻¹ under 15° slope, respectively in Fig. 3 a and b. Analysis of paired photos and runoff samples showed a 0.5 to 3 min lag between sidewall failure and increased sediment delivery. Small steady rates of sediment delivery during the low transport period (Fig. 3) were attributable to toe scour which facilitated channel widening during the high transport period (Fig. 4). One treatment (4 cm initial channel width, 4 L min⁻¹ inflow rate at 15° bed slope) was selected to analyze the relationship among sediment discharge rate, number of failure blocks and failure block size (Fig. 5). The sediment discharge rate significantly increased after the first failure block occurred at 4 min. Obviously, the sediment peak occurred with a 1 to 2 min lag of larger column presence, which might be attributed to the entrainment and transport of the failed blocks.

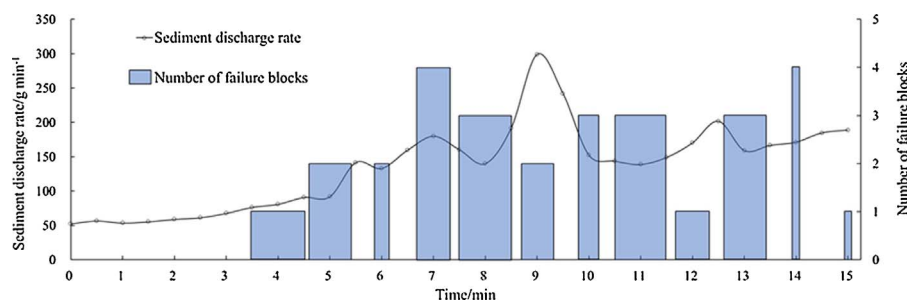


Fig. 5. Time series of sediment discharge rate, number of failure blocks and average surface area represented by block size of 4 cm initial channel width, 4 L min⁻¹ inflow rate at 15° bed slope treatment. The area of columns: $\bar{A} = l \times w$, where l represents the average length of failure blocks, w represents the average width of failure blocks.

3.3. Impacts of channel toe scour and tension crack on channel widening

Due to the shallow flow depth (0.05 to 0.18 cm) in all runs, only a small portion of the channel sidewall height (4 cm) was occupied by concentrated flow. The primary mode of channel widening initiation was characterized as erosion at the toe of the sidewall, followed by tension crack development and gravity induced cantilever failures (Wells et al., 2013). In this study, four periods are used to describe the channel widening processes: toe scour, crack development, sidewall failure and block detachment and transport (Table 3). Blocks of failed sidewall material fell into the flow and, in most cases, were transported downstream gradually, resulting in large sediment delivery fluctuations (Fig. 3). However, basal undercutting, arc length and arc height were relatively constant if no new cracks formed. Parameters of channel toe scour and crack development are discussed further in the following section.

3.3.1. Basal undercutting, arc length and height

During the progression from concentrated flow scour to sidewall failure, basal undercutting, arc length and height showed different development trends. Typical scour examples, selected from Run 1, 5 and 9 due to extended development, are shown in Fig. 6. In general, basal undercutting and arc length increased, while basal scour height initially increased then decreased as the process went on (Fig. 6). The evolution time of channel toe scour and crack development was more than seven times that of sidewall failure (Fig. 6 and Table 3). After the first sidewall failure, toe scour and block transport occurred simultaneously. Basal undercutting, arc length and height kept relatively constant due to the obstruction of failed block and dispersion of soil particles (Figs. 1 and 7). The decrease in scour height may be attributed to soil slaking, block size and cohesive binding of the material. As the potential failure block increased in length, there was more surface area to resist complete failure while the sidewall toe was subjected to further attack. The mass of the potential failure block was sufficient to keep the block in place as the flowing water at the toe wetted the material and induced slaking.

Basal undercutting, arc length and basal scour height (the maximum during the whole process) increased when the inflow rate and slope gradient increased, and when initial channel width decreased (Table 4). Basal undercutting for 4 cm initial channel width increased by 13.4% at 15° slope gradients and 28.6% at 20° slope gradients, when inflow rate increased from 1 to 4 L min⁻¹. With an initial channel width of 8 cm at

Table 3
Processes used to describe channel expansion.

Widening process	Sediment delivery	Channel width	Duration
Toe scour	Increase slight	Keep stable	Long
Crack development	Keep stable	Keep stable	Medium
Sidewall failure	Keep stable	Increase sharply	Short
Block transport	Increase sharply	Keep stable	Medium

Note: After the first sidewall failure event, circles of “toe scour-sudden failure-fast removal of fallen material-exhaustion of fallen material-toe scour-another sidewall failure” occurred.

20° slope gradient, basal undercutting increased by 18.8% when the inflow rate increased from 1 to 4 L min⁻¹. Basal scour depth was correlated to experimental parameters (i.e., flow rate and slope), which could signify critical basal undercutting to some extent, given experimental boundaries. Wang et al. (2016) indicated that when caving erosion width (in a river bank stability study) was larger than a critical value, cantilever failures such as shear, toppling and stress failures may occur. Compared to basal undercutting, the effects of flow rate on basal scour arc length and height were much more significant. Basal scour arc length and height increased by 67.1% to 73.2% and 50.0% to 72.8% when inflow rate increased from 1 to 4 L min⁻¹, respectively. These results are consistent with those given by Chen et al. (2013), where maximum scour depth and height of a gully sidewall increased with accumulated flow and scouring time in the Yuanmou Valley region, China.

3.3.2. Basal scour arc types

Though the top surface failure arcs showed similar crescent shapes with each other (Fig. 7), the basal scour arcs (96 samples from 12 treatments including two replicates), measured at the interface with the non-erodible layer, exhibited a range of geometries (Fig. 7). The differences between basal scour arcs and failure arcs could be attributed to the time lag between the process of sidewall failure and toe scour. The obstruction of failed blocks also impacted the flow velocity, width, depth and shear stress. The formation of new basal scour arcs, the number of failure blocks, intervals between two failures and sediment delivery may be influenced by the obstruction (Chaplot, 2013). In general, the number of sidewall failures was the same as the number of basal scour arcs (Table 5). However, the above two numbers were not always consistent because the secondary sidewall failure was not strictly consistent with the basal scour arcs. Three distinct types of scour arcs were detected in these experiments: normal, surface and reverse (Fig. 7). The normal scour arc shape (A) was similar to that of the surface failure arc and promoted secondary sidewall failure. The reverse scour arc (B) was divergent to the failure block, in the respect that basal scour was detected much deeper into the channel sidewall than that of the potential failure block. Large amounts of overhanging soil were observed on the upstream and downstream sidewalls behind failed blocks. The surface arc shape (C) was approximately parallel to the channel sidewall. Surface runoff flowed parallel to the channel toe so that no vortex flow formed. Basal undercutting increased slowly and the time interval for secondary failure was longer than that of the normal scour arc. Among 96 scour arcs in total, the occurrence frequency of scour arc types was, in descending order, normal (78 times), surface (10 times) and reverse (8 times). When calculating hydrodynamic parameters of channel concentrated flow, basal scour arcs, caused by basal undercutting, should be considered due to their impact on channel cross-sections. Varied channel cross-sections, usually caused by the difference between channel top and bottom widths (Kompani-Zare et al., 2011; Fiorucci et al., 2015), may result in different channel flow depth, width and velocity. To gain accurate near-sidewall channel flow parameters, underneath topography need to be measured manually or by using laser scanner as a supplementary for photogrammetry and remote sensing.

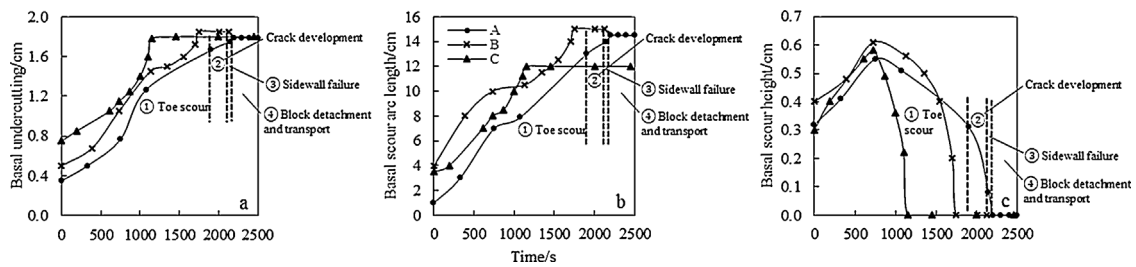


Fig. 6. General development of a) basal undercutting (U_b), b) basal scour arc length (L_b) and c) basal scour height (H_b) during channel widening. Examples are selected from one particular run due to extended development: A) Run 1 from 9 min 31 s to 51 min 11 s, B) Run 5 from 3 min 50 s to 39 min 15 s, and C) Run 9 from 4 min 20 s to 45 min 14 s. Dashed lines distinguish four periods of channel widening: channel toe scour, crack development, sidewall failure and block detachment and transport of Run 1.

3.3.3. Basal scour mechanisms

Although there was no direct influence of channel toe scour on channel widening measured during the experiment, the process of toe scour facilitated the development of tension cracks and sidewall failure (Table 3). The sediment source in the early phase of the experiments was the channel toe scour caused by concentrated flow erosion (Figs. 1 and 2). At the beginning of channel widening, sidewall sediment was directly entrained by the concentrated flow. During channel toe scour, the basal scour height and the mass of hanging soil increased (Figs. 2 and 6). As time progressed and surface runoff continued to erode the channel toe, gravity began to exceed the cohesive binding of the sidewalls and tension cracks evolved (Figs. 1 and 2). The infiltration of flowing water in contact with sidewall facilitated: 1) the driving forces increase due to the increased weight of the soil mass and 2) the resistance forces decrease due to the decreased shearing resistance of the soil mass (Bradford and Piest, 1977; Hossain et al., 2011). Sidewall failure followed, as sediment slid down the failure plane or toppled toward the channel bed, providing another sediment source for runoff transport (mass failure) (Figs. 1 and 7).

3.3.4. Tension crack variations

Tension cracks tend to decrease the overall stability of the channel sidewall by reducing cohesion and, often resulting in failure or contributing to topping (Martinez-Casasnovas et al., 2004; Istanbuluoglu et al., 2005; Thomas et al., 2009). The occurrence of tension cracks signified the initiation of channel widening (Fig. 1). Fig. 8 shows that both crack length and width increased as time increased. The crack widening rate was highest during the high transport period. Generally speaking, both the ultimate crack length and lengthening rate increased with increased inflow rate, slope gradient and declined with the increase of initial channel width (Table 4). This finding could be attributed to the increase of basal scour arc length (Table 4). Ultimate crack length increased by 7.0% to 22.2% and 16.5% to 100.6% when inflow rate increased from 1 to 2 L min⁻¹ and 2 to 4 L min⁻¹, respectively, and

Table 4

Average measurements of eight selected basal scours and tension cracks along channel sidewall for different experimental runs.

Run	U_b/cm		L_b/cm		H_b/cm		L_c/cm		$V_{cl}/cm\ min^{-1}$	W_c/cm		$V_{cw}/cm\ min^{-1}$
	Avg	SD	Avg	SD	Avg	SD	Avg	SD		Avg	SD	
1	1.9	0.3	13.8	8.3	0.6	0.1	9.1	2.5	2.6	1.2	0.3	0.4
2	1.9	0.6	15.8	11.7	0.7	0.2	9.7	3.0	4.4	1.3	0.3	1.0
3	1.9	0.6	19.6	2.6	1.0	0.2	16.3	5.5	7.2	1.5	0.4	1.1
4	2.1	0.7	23.8	11.4	0.9	0.0	16.6	5.3	9.6	1.5	0.2	1.2
5	1.8	0.2	15.6	7.9	0.6	0.2	13.0	3.6	3.4	1.3	0.2	0.4
6	2.1	0.3	17.3	10.4	0.7	0.2	15.7	3.7	7.0	1.3	0.4	1.1
7	2.2	0.5	17.8	8.5	0.8	0.1	17.1	4.9	7.5	1.5	0.6	1.2
8	2.3	0.2	26.0	8.5	0.9	0.1	18.3	8.2	9.7	1.4	0.4	1.2
9	2.0	0.3	9.9	4.2	0.5	0.1	7.2	0.9	1.8	1.2	0.5	0.4
10	2.1	0.4	10.0	4.0	0.7	0.2	8.9	4.2	3.7	1.2	0.4	0.7
11	2.2	0.3	12.4	3.9	0.8	0.1	16.0	8.1	7.9	1.5	0.3	1.0
12	2.4	0.4	17.1	7.5	0.9	0.2	17.8	2.8	9.5	1.5	0.2	1.5

decreased by 2.7% to 44.3% when initial channel width increased from 4 to 8 cm. The increase in crack lengthening rate could be attributed to the decrease in time from crack formation to sidewall failure when the inflow rate and slope gradient increased or channel width decreased. A similar trend was found for ultimate crack width and widening rate.

3.4. Sediment delivery disaggregation

Assuming channel sidewall failure can be attributed to a combination of concentrated flow erosion at the sidewall toe (concentrated flow shearing processes) and gravitational erosion (gravitational mass failure processes), sediment delivery may be described as a combination of concentrated flow and gravitational components as:

$$S = E_c + E_g \tag{4}$$

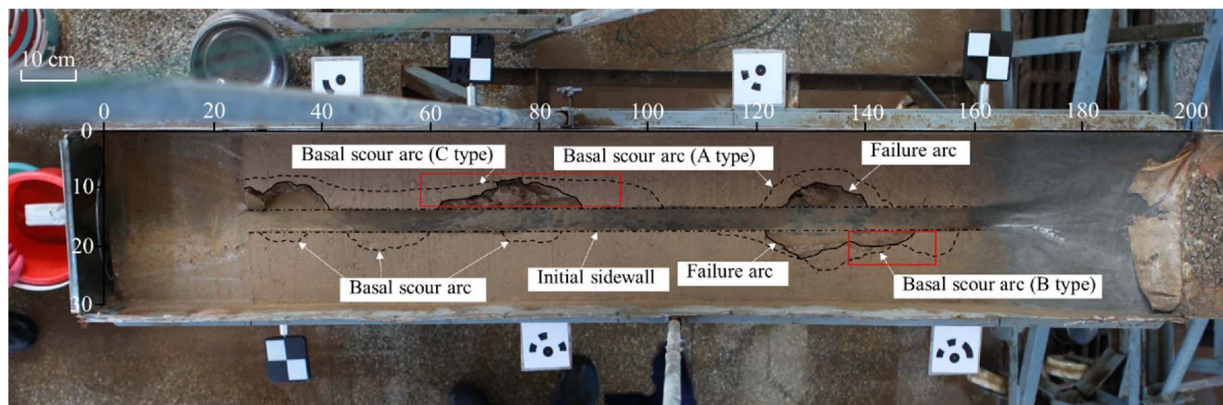


Fig. 7. Different types of basal scour arc (A type: normal, B type: reverse, C type: surface) and failure arc (from top view). Dash-and-dot lines represent initial channel sidewall, solid lines represent failure arc and dashed lines represent basal scour arc (cannot be seen from the top view, they were measured manually).

Table 5
Measured data used in the disaggregation simulation.

Run	N	n	A_s/cm^2	E_c/kg	E_g/kg	S_{sd}/kg	$P/\%$
1	11	10	10.2	0.09	0.43	0.51	83
2	13	13	12.5	0.15	0.59	0.74	80
3	14	15	28.9	0.29	1.33	1.62	82
4	15	15	31.0	0.36	1.60	1.96	82
5	12	11	18.9	0.11	0.85	0.96	89
6	14	15	22.5	0.20	1.14	1.34	85
7	16	16	27.7	0.29	1.54	1.83	84
8	17	18	35.3	0.50	2.05	2.55	80
9	12	11	11.9	0.07	0.54	0.61	88
10	15	14	14.8	0.12	0.80	0.92	87
11	15	16	21.7	0.17	1.15	1.33	87
12	16	15	35.3	0.33	1.90	2.24	85

Note: N is the number of basal scour arcs; n is the number of sidewall failures; A_s is the failed block surface area; E_c is the soil loss caused by concentrated flow erosion; E_g is the gravity erosion; S_{sd} is the simulated sediment delivery; P is the contribution of gravity erosion to sediment delivery.

where S is the sediment delivery (kg), E_c is the soil loss caused by concentrated flow erosion (kg), and E_g is the soil loss caused by gravity erosion (kg).

The concentrated flow erosion component consists of soil particles entrained by concentrated flow, a result of basal undercutting (i.e., toe scour effects). Assuming that the eroded mass from toe scour may be approximated by as a triangular prism, E_c may be expressed as:

$$E_c = 0.5 \times U_b \times L_b \times H_b \times \rho \times N \times 0.001 \quad (5)$$

where U_b is the basal undercutting (cm), L_b is the basal scour arc length (cm), H_b is the basal scour height (cm), ρ is the soil bulk density of the plow layer (g cm^{-3}), N is the number of basal scour arcs, and 0.001 is a unit conversion factor (g to kg).

Further, erosion by gravitational failure may be assumed to approximate a prism, where E_g may be expressed as:

$$E_g = A_s \times (H_i - H_b) \times \rho \times N \times 0.001 \quad (6)$$

where A_s is the failed block surface area (cm^2) and H_i is the initial channel sidewall height (cm).

Substituting Eqs. (5) and (6) into Eq. (4), yields:

$$S = (0.5 \times U_b \times L_b \times H_b + A_s \times (H_i - H_b)) \times \rho \times N \times 0.001 \quad (7)$$

Values used to evaluate Eq. (7) are provided in Tables 2, 4 and 5 and soil bulk density was 1.10 g cm^{-3} . Measured sediment delivery values (M_{sd}) were plotted against simulated sediment delivery estimates (S_{sd}) from Eq. (11) for each experiment ($S_{sd} = 1.23M_{sd} - 0.32$; $n = 12$; $R^2 = 0.95$). The average absolute difference (ϵ) between measured and calculated sediment delivery was 12.9% with a standard deviation (σ) of 10.9. Several optimization schemes were implemented to investigate the error, including: universal change in bulk density ($\epsilon = 12.7\%$, $\sigma = 10.6$); individual run adjustable bulk density ($\epsilon = 0\%$; $\rho_{\text{avg}} = 1.17$, $\sigma = 0.21$); average individual run bulk density ($\rho = 1.15$)

with adjustable erosion parameters confined by standard deviation ($\epsilon = 2.95\%$, $\sigma = 5.01$); and adjustable bulk density with adjustable erosion parameters confined by standard deviation ($\epsilon = 0.0\%$).

Allowing a universal adjustment to bulk density does not help explain the error; however, significant improvement was obtained when bulk density was allowed to adjust for each experiment. Overall, the bulk density value increased to an average of 1.17 g cm^{-3} with a σ_b of 0.21. Runs 1 and 2 (1.61, 1.50) had the highest values and Runs 8 and 12 (0.98, 0.94) had the lowest values. When bulk density was assumed to be a constant (1.15 g cm^{-3}) and the erosion parameters were allowed to adjust within the confines of the standard deviation of the measurements, the error was confined to Runs 1, 8, 9, and 12. The solution error was contingent upon the bulk density and, when bulk density was allowed to adjust for these outlier experiments, Runs 1 and 9 (1.34, 1.20) increased by 0.15 and Runs 8 and 12 (1.07, 1.06) decreased slightly. This analysis does show that, within the context of an overland flow in the absence of rainfall, the formulation (Eq. (7)) does have merit as a means to disaggregate the processes represented in sediment delivery.

The results show that the number of basal scour arcs and failed block surface area increased with the increased inflow rate and slope gradient, and the decreased initial channel width (Table 5). Soil loss caused by concentrated flow erosion and gravity erosion showed the same trend. However, the contribution of gravity erosion to sediment delivery increased with the decrease of inflow rate and increase of slope gradient. Initial channel width had little effect on the contribution of gravity erosion. The gravitational contribution was greater than 80%, which implies that concentrated flow erosion (basal scour), although not a significant contributor to sediment delivery, does create the necessary conditions ultimately responsible for channel widening, by fundamentally instigating the collapse of the hanging layers (Chen et al., 2013). This finding was different in comparison to the results of Chaplot et al. (2011), who indicated that the fall down of aggregates only contributed 13% of overall erosion rate when simulated rainfall experiments were conducted. This could be possibly attributed to the vertical nature of loess and the severe gravity erosion on the Loess Plateau. Blong et al. (1982) discussed three processes that contributed to gully sidewall development: linear incision, sidewall erosion, throughout flow and overland flow erosion. With the investigation of four typical gullies in New South Wales, Australia, these authors pointed out that more than half of the gully volume could be attributed to sidewall erosion (gravitational erosion) while another 10% originated from overland flow and throughflow processes. The results of this study verified their data.

4. Conclusions

Laboratory channel expansion tests were performed to study the effect of flow rate, slope gradient and initial channel width on sediment delivery and channel widening processes. The preformed channel simulated a field condition where an initial headcut erodes to a non-

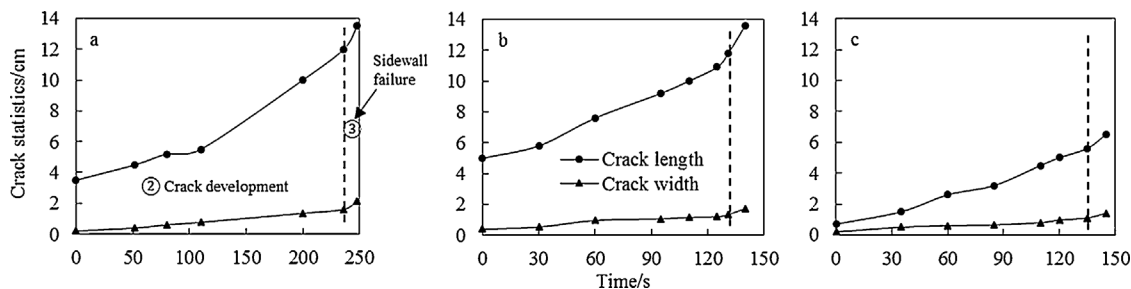


Fig. 8. General dimensions of crack development (crack length (L_c) and average crack width (W_c)) from tension crack formation to sidewall failure. Examples are selected from one particular run due to extended development: a) Run 1 from 9 min 31 s to 51 min 11 s, b) Run 5 from 34 min 10 s to 36 min 30 s, and c) Run 9 from 24 min 10 s to 26 min 45 s. Dashed lines represent the boundary between crack development and sidewall failure.

erodible layer as it advances upstream, exposing channel sidewalls downstream of the headcut to concentrated flow. Sediment delivery and unit sediment delivery increased with the increase of inflow rate, slope gradient and initial channel width decrease. Toe scour, crack development, sidewall failure and block detachment and transport were the four main widening processes observed. Sediment delivery and channel width were different during each phase of the channel widening process. Channel toe scour processes were continuous while the sidewall failure process occurred episodically. Time lag could be detected between sediment peak and soil block failure (Fig. 5). Exponential equations using the initial channel width were used to simulate the channel width time series. Except for basal scour height, other indicators including basal undercutting, arc length and crack length and width increased with time. Three types of basal scour arc were identified and their occurrence frequency, in descending order, were normal type, surface type and reverse type. The difference between failure arcs and basal scour arcs should be considered when calculating hydrodynamic parameters due to their impact on channel cross-sections. Sediment delivery was decomposed into concentrated flow erosion and gravity erosion, and fitted equations of sediment delivery were presented. Results of this study provide new knowledge related to understanding and prediction of channel widening processes. Prevention practices should focus upon the four main channel widening processes to improve channel sidewall stability.

Acknowledgments

This study was supported by the National Natural Science Foundation of China (No. 41271299, 4171101192), Opening Funds of MWR Key Laboratory of Soil and Water Loss Process and Control in the Loess Plateau (No. 2017001), Special-Funds of Scientific Research Programs of State Key Laboratory of Soil Erosion and Dryland Farming on the Loess Plateau (A314021403-C2), External Cooperation Program of Chinese Academy of Sciences (161461KYSB20170013) and China Scholarship Council funds. The authors would like to thank Dr. Glenn V. Wilson and Dr. Seth M. Dabney for early review comments.

References

- Billi, P., Dramis, F., 2003. Geomorphological investigation on gully erosion in the Rift Valley and the northern highlands of Ethiopia. *Catena* 50, 353–368.
- Bingner, R.L., Wells, R.R., Momm, H.G., Rigby, J.R., Theurer, F.D., 2016. Ephemeral gully channel width and erosion simulation technology. *Nat. Hazards* 80, 1949–1966.
- Blong, R.J., Graham, O.P., Veness, J.A., 1982. The role of sidewall process in gully development; some N.S.W. example. *Earth Surf. Processes Landforms* 7, 381–385.
- Bradford, J.M., Pies, R.F., 1977. Gully wall stability in loess-derived alluvium. *Soil Sci. Soc. Am. J.* 41 (1), 115–122.
- Castillo, C., Gómez, J.A., 2016. A century of gully erosion research: urgency, complexity and study approaches. *Earth Sci. Rev.* 160, 300–319.
- Chaplot, V., Brown, J., Dlamini, P., Eusticec, T., Janeau, J., Jewitt, G., Lorentz, S., Martinc, L., Nontokozo-Mchunue, C., Oakes, E., Podwojewskia, P., Revild, S., Rumpel, C., Zondid, N., 2011. Rainfall simulation to identify the storm-scale mechanisms of gully bank retreat. *Agric. Water Manage.* 98, 1704–1710.
- Chaplot, V., 2013. Impact of terrain attributes, parent material and soil types on gully erosion. *Geomorphology* 186, 1–11.
- Chen, A., Zhang, D., Peng, H., Fan, J., Xiong, D., Liu, G., 2013. Experimental study on the development of collapse of overhanging layers of gully in Yuanmou Valley, China. *Catena* 109, 177–185.
- Dabney, S.M., Vieira, D.A.N., Yoder, D.C., Langendoen, E.J., Wells, R.R., Ursic, M.E., 2014. Spatial distributed sheet, rill, and ephemeral gully erosion. *J. Hydrol. Eng.* 20 (6) (C4014009-1-C4014009-12).
- Darby, S.E., Alabyan, A.M., Van de Wiel, M.J., 2002. Numerical simulation of bank erosion and channel migration in meandering rivers. *Water Resour. Res.* 38 (9) 2-1–2-21.
- Di Stefano, C., Ferro, V., 2011. Measurements of rill and gully erosion in Sicily. *Hydrol. Processes* 25, 2221–2227.
- El Kadi Abderrezak, K., Die Moran, A., Mosselman, E., Bouchard, J., Habersack, H., Aelbrecht, D., 2014. A physical, movable-bed model for non-uniform sediment transport, fluvial erosion and bank failure in rivers. *J. Hydro-Environ. Res.* 8, 95–114.
- FAO (Food and Agriculture Organization, 1965. *Soil Erosion by Water. Some Measures for Its Controls on Cultivated Lands.* Agriculture Paper, 81. (Rome).
- Fiorucci, F., Ardizzone, F., Rossi, M., Torri, D., 2015. The use of stereoscopic satellite images to map rills and ephemeral gullies. *Remote Sens.* 7, 14151–14178.
- Foster, G.R., Lane, L.J., Nowlin, J.D., Laflen, L.M., Young, R.A., 1980. A Model to Estimate the Sediment Yield from Field-sized Areas: Development of Model and Selection of Parameters Values. CREAMS: A Field Scale Model for Chemicals, Runoff, and Erosion from Agricultural Management Systems. Conservation Research Report, 26. U.S. Department of Agriculture, pp. 36–64 193–281.
- Foster, G.R., 1986. Understanding Ephemeral Gully Erosion. Committee on Conservation Needs and Opportunities, Soil Conservation Ed., Assessing the National Resources Inventory, Board on Agriculture, National Research Council. National Academy Press, Washington, DC, pp. 90–125.
- Fullen, M.A., 1985. Compaction, hydrological processes and soil erosion on loamy sands in east Shropshire, England. *Soil Tillage Res.* 6, 17–29.
- Gordon, L.M., Bennett, S.J., Wells, R.R., Alonso, C.V., 2007. Effect of soil stratification on the development and migration of headcuts in upland concentrated flows. *Water Resour. Res.* 43 (W07412), 1–13.
- He, J., Li, X., Jia, L., Gong, H., Cai, Q., 2014. Experimental study of rill evolution processes and relationships between runoff and erosion on clay loam and loess. *Soil Sci. Soc. Am. J.* 78 (5), 1716–1725.
- Hossain, M.B., Sakai, T., Hossain, M.Z., 2011. River embankment and bank failure: a study on geotechnical characteristics and stability analysis. *Am. J. Environ. Sci.* 7 (8), 102–107.
- Hunt, C.M., Woolf, A.R., 1969. Comparison of some different methods for measuring particle size using microscopically calibrated glass beads. *Powder Technol.* 3 (1), 9–23.
- Istanbulluoglu, E., Bras, R.L., Flores-Cervantes, H., Tucker, G.E., 2005. Implications of bank failures and fluvial erosion for gully development: field observations and modeling. *J. Geophys. Res.* 110 (F01014), 1–21.
- Kompani-Zare, M., Soufi, M., Hamzehzarghani, H., Dehghani, M., 2011. The effect of some watershed, soil characteristics and morphometric factors on the relationship between the gully volume and length in Fars Province, Iran. *Catena* 86, 150–159.
- Liu, G.S., 1996. *Soil Physical and Chemical Analysis and Description of Soil Profiles.* Standards Press of China, Beijing, pp. 7–32 (in Chinese).
- Martinez-Casasnovas, J.A., Ramos, M.C., Poesen, J., 2004. Assessment of sidewall erosion in large gullies using multi-temporal DEMs and logistic regression analysis. *Geomorphology* 58, 305–321.
- Momm, H.G., Wells, R.R., Bingner, R.L., 2015. GIS technology for spatiotemporal measurements of gully channel width evolution. *Nat. Hazards* 79, S97–S112.
- Nash, J.E., Sutcliffe, J.V., 1970. River flow forecasting through conceptual models part I. A discussion of principles. *J. Hydrol.* 10 (3), 282–290.
- Poesen, J.W., Nachtergale, J., Verstraeten, G., Valentin, C., 2003. Gully erosion and environment change: importance and research needs. *Catena* 50, 91–134.
- Särndal, C., Swensson, B., Wretman, J.H., 1992. *Model Assisted Survey Sampling.* Springer-Verlag, New York.
- Santhi, C., Arnold, J.G., Williams, J.R., Hauck, L.M., Dugas, W.A., 2001. Application of a watershed model to evaluate management effects on point and nonpoint source pollution. *Trans. ASAE* 44 (6), 1559–1570.
- Shen, H., Zheng, F., Wen, L., Lu, J., Jiang, Y., 2015. An experimental study of rill erosion and morphology. *Geomorphology* 231, 193–201.
- Simon, A., Rinaldi, M., Hadish, G., 1996. Channel evolution in the loess area of the midwestern United States. In: *Proceedings, Sixth Federal Interagency Sedimentation Conference.* Las Vegas, March 10–14. pp. III-86–III-93.
- Thomas, J.T., Iverson, N.R., Burkart, M.R., 2009. Bank-collapse process in a valley-bottom gully, western Iowa. *Earth Surf. Processes Landforms* 34, 109–122.
- USDA NRCS, 1999. *Soil Taxonomy: A Basic System of Soil Classification for Making and Interpreting Soil Surveys.* Agric. Handbook 436, 2nd edition. U.S. Government Printing Office, Washington, DC.
- Wang, Y., Shao, M.A., Liu, Z., Zhang, C., 2014. Prediction of bulk density of soils in the Loess Plateau region of China. *Surv. Geophys.* 35 (2), 395–413.
- Wang, Y., Kuang, S., Su, J., 2016. Critical caving erosion width for cantilever failures of river bank. *Int. J. Sediment Res.* 31 (3), 220–225.
- Wells, R.R., Momm, H.G., Rigby, J.R., Bennett, S.J., Bingner, R.L., Dabney, S.M., 2013. An empirical investigation of gully widening rates in upland concentrated flows. *Catena* 101, 114–121.
- Wu, Y., Cheng, H., 2005. Monitoring of gully erosion on the Loess Plateau of China using a global positioning system. *Catena* 63 (2-3), 154–166.
- Zhang, H., 1983. The characteristics of hard rain and its distribution over the Loess Plateau. *Acta Geog. Sin.* 38 (4), 416–425 (in Chinese, with English Abstract).
- Zhou, P., Wang, Z., 1987. Soil erosion rainfall standard in the Loess Plateau. *Bull. Soil Water Conserv.* 7 (1), 38–44 (in Chinese, with English Abstract).